Available online at www.sciencedirect.com
ScienceDirect
Trans. Nonferrous Met. Soc. China 34(2024) 3862−3875
Transactions of Nonferrous Metals Society of China
www.tnmsc.cn

Microstructure and mechanical properties of complex-shaped 7075 aluminium alloy prepared using modified polyoxymethylene-based feedstock

Heng ZOU, Meng-xiong CHEN, Yang FU, Hui-wen XIONG, Lei ZHANG, Ke-chao ZHOU

State Key Laboratory of Powder Metallurgy, Central South University, Changsha 410083, China

Received 30 June 2024; accepted 25 November 2024

Abstract: Additives of dioctyl phthalate (DOP), ethylene bis-stearomide (EBS), and epoxy (EP) were selected to modify the surface of 7075 Al alloy powder. Functional groups in DOP and EBS form hydrogen bonds with hydroxyl groups on the surface of Al powder. Additionally, the epoxy groups in the epoxy resin undergo ring-opening reactions with hydroxyl groups. The above interactions increased the compatibility between alloy powder and polyoxymethylene (POM). After sintering, samples containing DOP and EP presented high contents of C and O, while the part with EBS additive exhibited the lowest contents of 0.006 wt.% C and 0.604 wt.% O, respectively. Excessive C tends to accumulate at grain boundaries during sintering. Concurrently, excessive O causes secondary oxidation of aluminium alloy powder, inhibiting the sintering densification process. Therefore, the densities of the samples containing DOP and EP were only 85.52% and 79.01%, respectively. In contrast, using EBS as an additive, high-quality aluminium alloy parts were achieved, with a relative density of 97.64% and a tensile strength of 193 MPa.

Key words: 7075 aluminium alloy; polyoxymethylene-based feedstock; additives; compression moulding; metal injection moulding; microstructure; mechanical properties

1 Introduction

7075 aluminum alloy is widely utilized in aerospace, industrial manufacturing, and other sectors requiring high-strength structural materials due to its excellent specific strength, good corrosion resistance, and wear resistance [1−3]. With the rapid advancements in smartphones, semiconductors, and other fields, the demand for lightweight and high-strength components continues to rise [4,5]. Metal injection molding of aluminium alloys (MIM-Al) has garnered significant attention due to its benefits of high dimensional accuracy, uniform structure, efficient raw material utilization, and superior performance [6,7]. The process involves adding a binder to the powder, which fills the inter-particle voids and enhances the fluidity during the molding. After removing the binder through one- or two-step debinding process, a densified structure is formed by sintering at high temperatures. The design of the binder is crucial in the injection molding process [8,9]. The binder typically comprises three parts: (1) the matrix, constituting 60−90 wt.% of the total binder, providing the necessary fluidity for feedstock; (2) the backbone, constituting 8−35 wt.% of the binder, providing strength for the green body; (3) additives, constituting 1−5 wt.% of the total binder, used to enhance the affinity between the powder and the binder, reduce molecular entanglement friction among binder components, and improve powder stability during injection [10,11]. However, at relatively low temperatures, the carbon and oxygen impurities

Corresponding author: Hui-wen XIONG, Tel: +86-15387311652, E-mail: huiwenxiong@csu.edu.cn
DOI: 10.1016/S1003-6326(24)66644-6

remaining after debinding can easily react with aluminium, which poses a significant challenge [12]. Therefore, the requirements for good rheology and low residue must be considered in the design of binders for MIM-Al [13−15].

Currently, wax-based binder systems are commonly used in MIM-Al, with stearic acid (SA) as the primary additive [16]. NI et al [17] prepared MIM-Al with a tensile strength of 154 MPa using a binder system consisting of carnauba wax (CW), high density polyethylene (HDPE), and SA. Furthermore, DAYAM et al [18] achieved aluminium alloys with a relative density of 98.24% by adding vaseline as a plasticizer. Nevertheless, with the widespread use of wax-based binders, their drawbacks have become apparent. For instance, the low viscosity of wax and significant volume changes during cooling could lead to defects such as phase separation and deformation. Moreover, solvent debinding of wax-based binder usually causes the billet to be prone to collapse [19−21]. Hence, finding a new binder is a crucial task for MIM-Al. Polyoxymethylene (POM)-based binders offer advantages including high debinding efficiency, good shape conformity, low residue and satisfactory dimensional accuracy, which have been successfully adopted in titanium alloys [22,23]. However, the study on POM-based binders for MIM-Al remains limited. One reason is the poor compatibility between POM and aluminium alloy powder, leading to non-uniform powder distribution in the binder [24]. Based on this, enhancing the wettability between POM and Al alloy powder is an efficient path [25]. Similar to active metal powders, the design of POM-based binder can draw on the MIM-Ti to a certain extent. LIU et al [26] investigated the effect of different active agents on the compatibility of TiAl powder injection moulding feedstock. The results showed that the addition of EBS resulted in a better wetting effect of the powder with the binder. CHEN et al [27] prepared Ti−6Al−4V−POM based feedstock using EBS as additive and prepared titanium alloy parts with a relative density of 97.10% and a tensile strength of 746 MPa.

This study aims to identify an optimal additive for MIM-Al in the context of POM-based feedstocks, with the goal of enhancing compatibility and improving the properties of the resulting processed products. Based on this, three additives of DOP, EBS, and EP were selected after investigating commonly used additives in titanium alloy metal powder injection molding [28]. Simultaneously, we proposed a facile powder compression molding process in which the feedstock was injected and compacted directly in the heated mould. This method helps prepare parts with complex shapes at relatively low processing costs due to the simplicity of the equipment [29]. We investigated the roles of additives in the morphology and viscosity of the POM-based feedstock, and studied the effect of C and O contents on the microstructure and mechanical properties of MIM-Al. Additionally, geometrically complex 7075 aluminum alloy was prepared by compression molding using the optimized binder system.

2 Experimental

2.1 Raw materials

The raw material powder was 7075 aluminium alloy powder (10 μm, Shanghai Xiangtian Nanomaterials Co., Ltd., China). The microscopic morphology of the powder is nearly spherical (as shown in Fig. S1 in Supplementary Materials). POM (DuPont, Shenzhen, China) was used as the main filler, and polypropylene (PP, Macklin, Shanghai, China) was selected as the backbone binder. Three different additives included the dioctyl phthalate (DOP, Sinopharm, Shanghai, China), ethylene bis-stearomide (EBS, Sinopharm, Shanghai, China), and epoxy (EP, Sinopharm, Shanghai, China), which were used to improve the wettability of the powder−binder mixture.

2.2 Compression moulding of 7075 aluminium alloy

The process of preparing 7075 aluminium alloy parts from POM by compression moulding (as shown in Fig. S2 in Supplementary Materials) involves four stages: mixing, forming, degreasing and sintering.

The volume fraction of 7075 aluminium alloy powder was maintained at 64%. The content of each component in the binder is presented in Table 1. Three groups of binders with different additives were designated as F1, F2, and F3 for the additives of DOP, EBS and EP, respectively. For the kneading process, aluminium alloy powder was added into the mixer chamber, set at 20 r/min,

heated to 110 °C and maintained for 2 h to ensure complete drying of the powder. Then, the temperature was raised to 190 °C, and POM-based polymer was added in increments to mix with the powder at a mixing speed of 40 r/min for 1 h. After that, the feedstock was cooled to room temperature to obtain the final material.

Table 1 Composition design of binders for 7075 Al-POM feedstock (wt.%)

Binder system	Main binder POM	Backbone binder PP	Additive		
			DOP	EBS	EP
F1	85	14	1	0	0
F2	85	14	0	1	0
F3	85	14	0	0	1

The pressureless sintering of the aluminum alloy was conducted in a tube furnace (GSL−1700X, Kejin, Hefei, China) under a high nitrogen flow, which established a low partial oxygen pressure to inhibit oxidation of the aluminum alloy powder and facilitated the breakdown of the oxide film on the powder surface [30]. The specific steps of the sintering process are as follows: (1) heating from room temperature at 2 °C/min to 350 °C for 1 h; (2) heating up at 1 °C/min to 450 °C for 1 h; (3) heating up at 1 °C/min to 500 °C for 1 h; (4) heating up to the final target temperature of 610 °C and holding for 1 h, and then cooling the chamber to room temperature. The entire process was conducted using high-purity nitrogen with a purity of 99.999% and a flow rate of 3 L/min.

2.3 Characterization

In order to evaluate the effect of different additives on the wettability of the aluminium alloy powder with POM, additives and 7075 powder were fully mixed by ball milling for 10 h. The contact angles of the three binders with aluminium alloy powders were measured using a contact angle meter (Dataphysics DCAT21, Germany) at 180 °C. The rheological properties of the three POM-based feedstocks were measured using a rotational rheometer (Haake Mars 60, Germany). The relationship between shear viscosity and shear rate of the feedstocks was determined at 180 °C and 10−1000 Pa. In order to gain a deeper understanding of the thermal decomposition properties and microstructural evolution of the 7075 aluminium alloy powder and the aluminium alloy-POM-based feedstocks, the thermal properties of the powders and feedstocks were characterized using TG−DTG (Netzsch STA2500, Germany). The microstructures of the powders, feedstocks, green bodies, degreased raw billets, and sintered alloys were observed using a scanning electron microscope (Mira3, Tescan, Czech) in combination with an EDS spectroscopic detector. The sintered densities of the alloys were measured using the Archimedes drainage method. Phase analysis of the sintered alloys was conducted via X-ray diffraction (XRD, X'Pert Pro MPD, Malvern Panalytical, Finland), and the tensile properties were evaluated using a universal testing machine (Instron 3369, USA).

3 Results and discussion

3.1 Effect of additives

A common method to improve the contact angle of the powder with the binder is the use of additives in the binder, which reduce the contact angle of the powder with POM through surface modification. Figure 1 shows the schematic diagram and results of the contact angle test. From Figs. 1(b−e), it can be seen that the contact angle between the original 7075 powder and POM reaches a maximum of 122.6°. After the addition of the additives, the contact angle between the powder and the binder is reduced, with the EBS-modified powder exhibiting the smallest contact angle with POM. This indicates that the powder and the binder have the best wettability at this point.

The surface of aluminium alloys typically contains a naturally occurring oxide layer, which

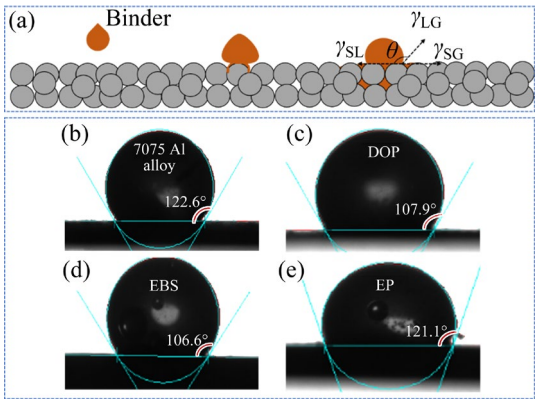

Fig. 1 Schematic diagram of contact angle experiment (a) and contact angle test results for different binder systems (b−e)

can further react with water or hydroxides to form hydroxyl groups (—OH) [31]. The addition of DOP, EBS, and EP may alter the intermolecular forces on the surface of aluminium alloy powders. This alteration affects the degrees of freedom and energy of molecular vibrations, thereby changing the positions of the infrared spectral peaks [32]. The infrared spectra in Fig. 2 show that the wavenumber positions of the O—H absorption peaks at 3784 and 3703 cm^{-1} in the free state decrease, and the peak shapes become broader after the addition of the additives. This suggests the presence of intermolecular or intramolecular interactions that facilitate bonding between the powders and the binder. Additionally, the wavenumber position of the C—O absorption peak at 1044 cm^{-1} in the original 7075 powder species increases after the additives are applied. The absorption peaks corresponding to C═O and C—N at 1403 cm^{-1} are also altered, indicating that the additives are evenly mixed with the surface of the aluminium alloy, thereby changing the positions of the infrared absorption peaks. The interactions of the three additives with the powder are illustrated in Fig. 3. DOP is a commonly used plasticizer. The oxygen atoms in its two ester groups are highly electronegative and act as hydrogen bond acceptors [33]. EBS, a commonly used lubricant, contains two amide groups in its molecular structure. The nitrogen and oxygen atoms in these groups possess lone pairs of electrons, enabling them to participate in hydrogen bonding [34]. Therefore, DOP and EBS adhere to the surface of aluminium alloy powders through hydrogen bonding. The epoxide (—CHOCH—) and hydroxyl (—OH) groups in epoxy resins can form new bonds (e.g., C—O—C or C—OH) through ring-opening reactions on the surface of aluminium alloy powders [35,36]. The resulting covalent bonds significantly enhance the adhesion between the epoxy resin and the aluminium alloy surface. The long alkane chain structures of EBS and DOP are similar to those of POM, and the epoxy groups in the epoxy resin can interact with the carbonyl groups in POM through intermolecular forces [37]. Therefore, the compatibility of the aluminium alloy powder with POM is enhanced by adding these additives during the mixing process.

3.2 Properties of 7075-POM feedstocks

3.2.1 Morphology and thermogravimetric curves

The morphologies and TG−DTG curves of the

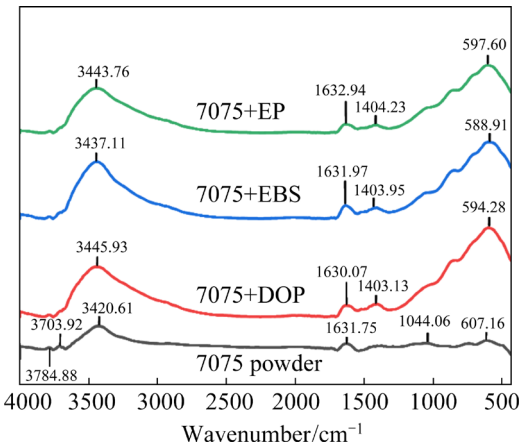

Fig. 2 Infrared spectra of original and modified powders

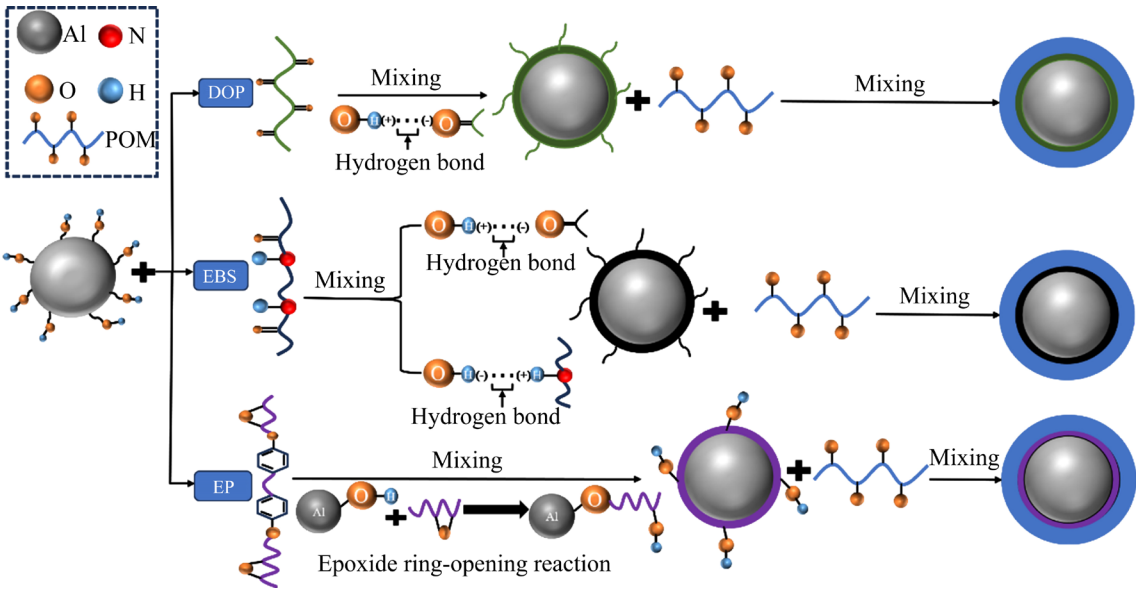

Fig. 3 Reaction mechanism between three additions and POM-based feedstock

feedstock are shown in Fig. 4. The binder is uniformly distributed around the powder, which potentially improves the mixture fluidity. In addition, this uniformity mitigates the risk of defects, such as cracks and deformation, which may arise from an excess of local binder during subsequent debinding and sintering processes. Figures 4(b, d, f) illustrate the TG−DTG curves of the three feedstocks. Initially, the TG curve shows a slight decrease before reaching 200 °C, likely due to the decomposition of water in the feedstock. As the temperature increases, the mass loss becomes significant starting at 200 °C. At 400 °C, the mass loss for F1, F2, and F3 samples is 22.99%, 19.97%, and 16.99%, respectively, corresponding to the total content of POM and additives in the feedstock. Notably, two distinct heat absorption peaks appear in the DTG curve between 350 and 440 °C, indicating the decomposition reactions of POM and PP. At 450 °C, a mass loss of approximately 2% is observed, which indicates the complete decomposition of PP. At 500 °C, the mass loss for F1, F2, and F3 samples reaches a maximum of 24.56%, 22.29%, and 18.69%, respectively.

3.2.2 Rheological properties of feed material

During the molding process, feedstocks typically exhibit pseudoplastic rheological behavior. The viscosity of the feedstock decreases as the shear rate increases when subjected to shear forces. This rheological property is crucial for the molding

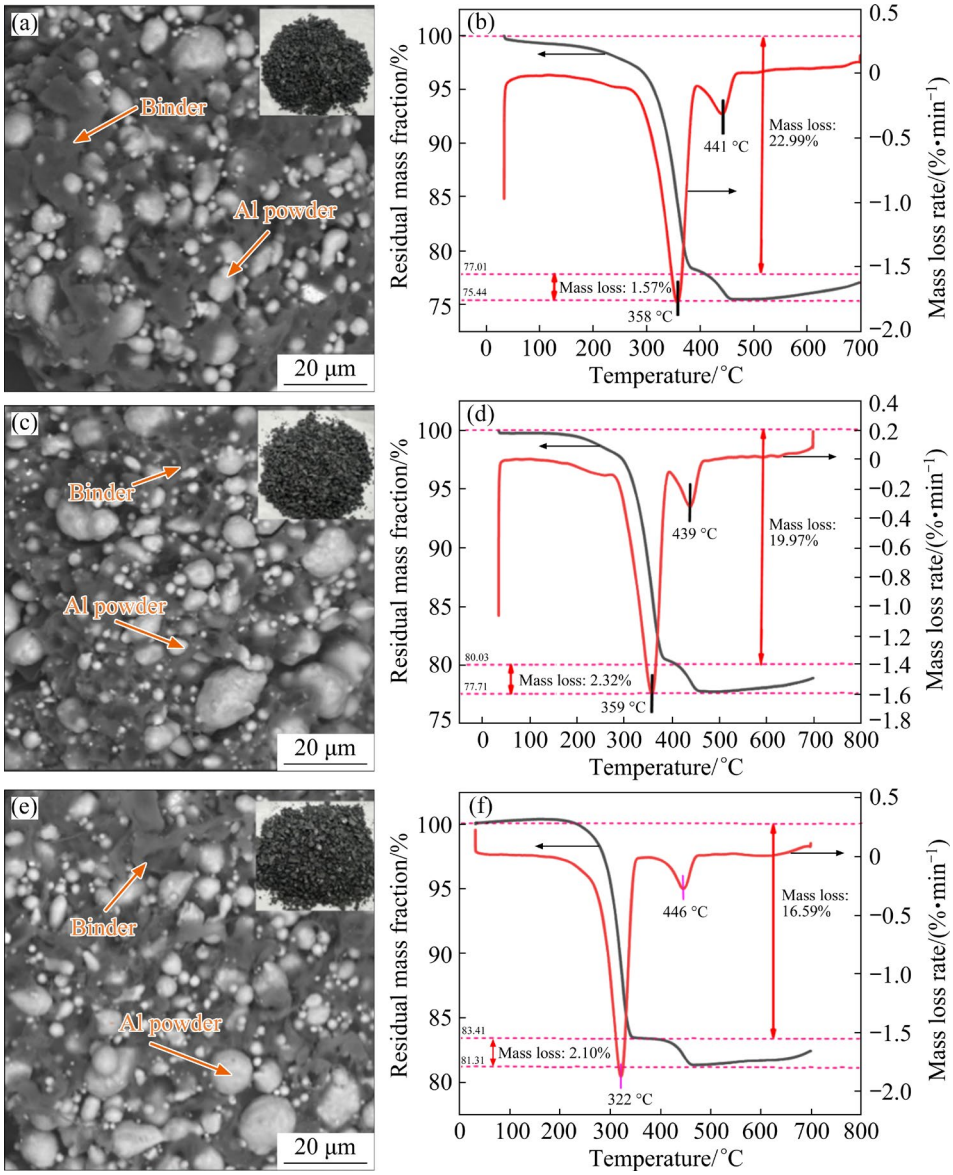

Fig. 4 SEM morphologies (a, c, e) and TG−DTG curves (b, d, f) of raw materials modified by different additives: (a, b) F1; (c, d) F2; (e, f) F3

process, as it enhances material flow and reduces the occurrence of defects, thereby improving the quality and consistency of the final product. The relationship between viscosity and shear rate can be expressed by the following equation [38]:

$$\eta=K\gamma^{n-1} \quad (1)$$

where η is the viscosity, K is a constant, γ is the shear rate, and n is the mobility index which reflects the fluid's shear sensitivity (usually $0.2<n<1$ is required, and the smaller the better). Figure 5 illustrates the relationship between shear stress and shear rate, as well as the logarithmic relationship between shear viscosity and shear rate. Figure 5(a) shows that with increasing shear rate, the shear stress increases. Figure 5(b) demonstrates that the feedstock exhibits the shear thinning pseudoplastic rheological behavior. This behavior results from the alteration of the original molecular chain composition under shear forces and the reorientation of molecular chains in the flow direction, leading to a decrease in viscosity [39].

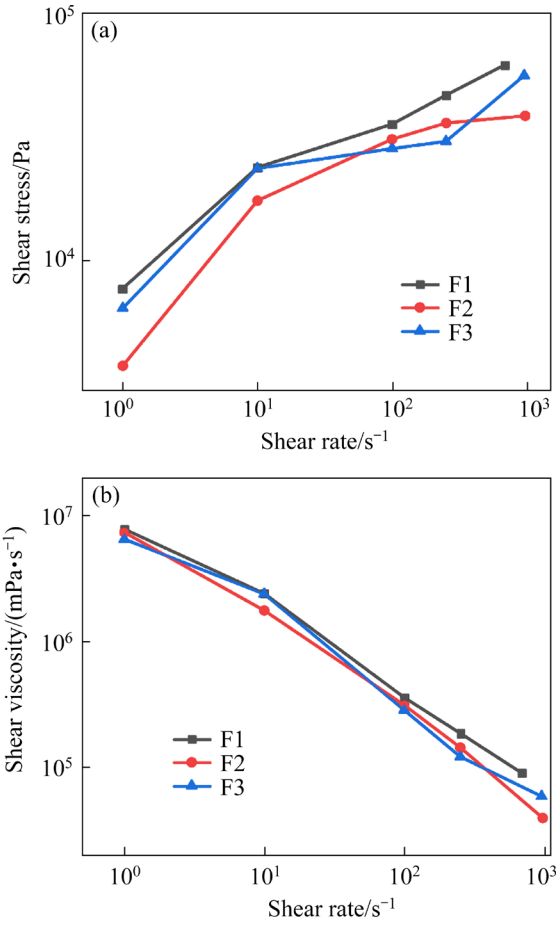

Fig. 5 Rheological curves of different samples: (a) Shear stress versus shear rate; (b) Shear viscosity versus shear rate

The non-newtonian indices (n) of the three feedstock groups (F1, F2 and F3) are 0.30, 0.25, and 0.27, respectively. This indicates that F2 exhibits the strongest pseudoplasticity, meaning that F2 experiences the most significant viscosity reduction under high shear rates, thereby possessing good fluidity.

3.3 Morphology of green body before and after forming and debinding

Approximately 36 vol.% of the binder in the billet was entirely removed during the debinding process. The model diagrams of the gears prepared by powder compression molding and the billets before and after debinding are shown in Fig. 6. Following debinding, the resulting porous structure of the billets is characterized by a network of inter-connected pores, which facilitates the subsequent sintering process.

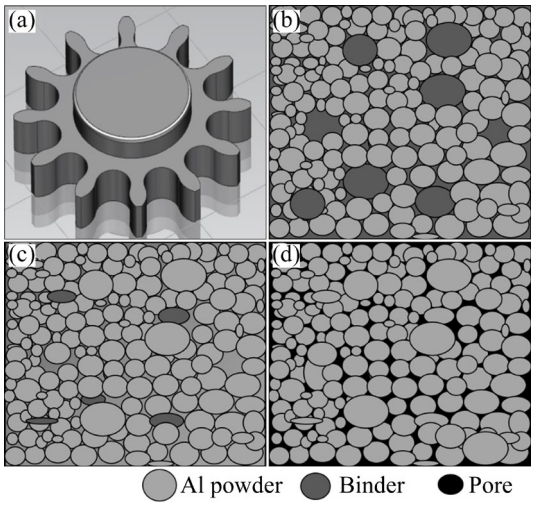

Fig. 6 Schematic diagrams before and after debinding of green body: (a) Gear model; (b) Green tissue model; (c) After catalytic debinding; (d) After thermal debinding

As shown in Fig. 7, the billets demonstrate high dimensional accuracy and smooth, defect-free surfaces, with the binder uniformly distributed in a mesh-like structure surrounding the powder particles. During catalytic debinding, the majority of the POM in the billet decomposes rapidly into small formaldehyde molecules, which are subsequently removed. The debinding temperature (120 °C) is maintained below the melting point of POM, effectively preventing the formation of a liquid phase. Under this condition, the billet retains its shape while developing porous spaces, which act as pathways for thermal debinding. As a result, the

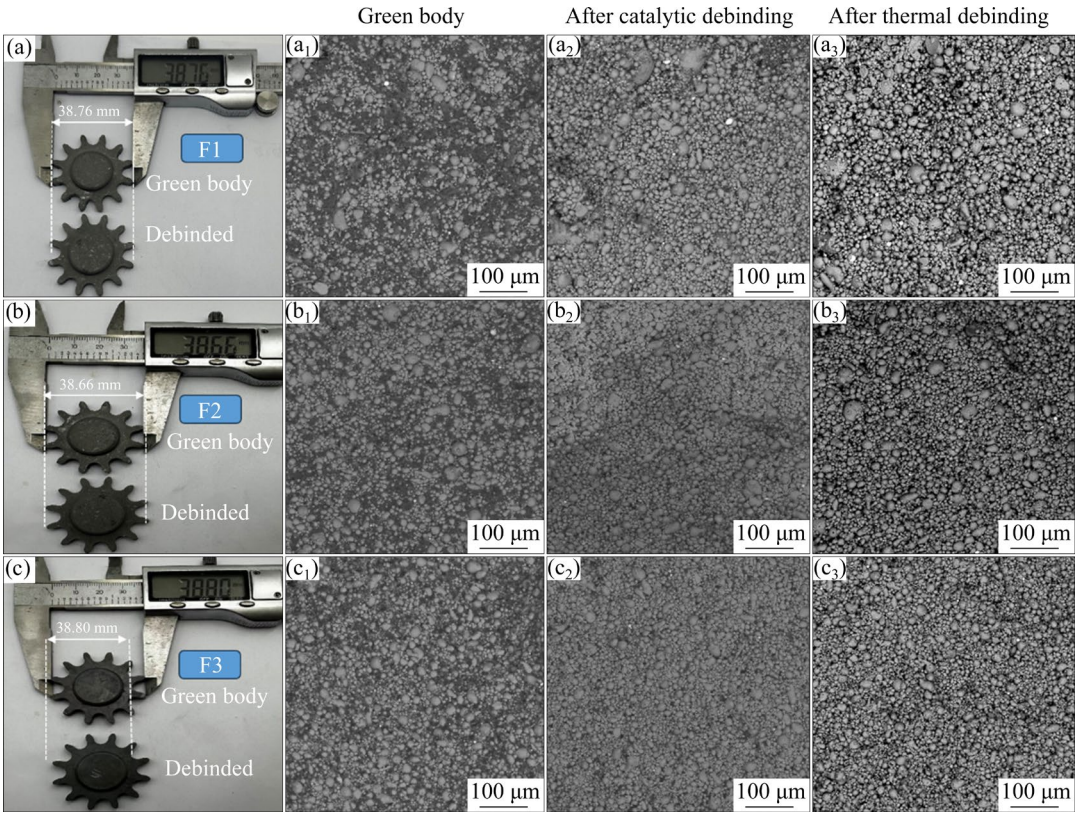

Fig. 7 Macroscopic morphologies (a, b, c) and SEM images (a_1−a_3, b_1−b_3, c_1−c_3) of green bodies before and after debinding: (a, a_1−a_3) F1 gear; (b, b_1−b_3) F2 gear; (c, c_1−c_3) F3 gear

billet surface remains smooth and dimensionally stable, showing no deformation or other defects.

3.4 Morphology of sintered aluminum alloy

The sintering process is critical in determining the overall performance of the final product. Aluminum alloy powder is highly reactive, forming a dense oxide film on its surface. To promote densification and prevent secondary oxidation, a high-flow nitrogen atmosphere is utilized during sintering. The morphology and microstructure of each group after sintering are presented in Fig. 8. The F1 and F3 samples display notable porosity and distinct grain boundaries, with densities of 85.52% and 79.01%, respectively. These findings suggest that substantial densification barriers were present, which hindered the formation of sintering necks and led to incomplete densification. The presence of pores negatively impacts the mechanical properties of the materials and may lead to instability during subsequent processing [40]. In contrast, the F2 samples exhibited filled pores and a dense structure after sintering, achieving a high density of 97.64%. This suggests effective metallurgical bonding, characterized by less prominent grain boundaries, which enhances the strength and toughness of the materials.

EDS analysis revealed that the C and O contents in the F1 and F3 samples were significantly higher than those in the F2 sample. This may be attributed to the accumulation of C and O at the pore boundaries, which creates an environment unfavorable for densification. In the F2 sample, however, the C and O elements were uniformly distributed, indicating effective control of carbon oxides during sintering, which facilitated alloy densification [41]. Additionally, the Cu, Mg, and Si elements tended to aggregate, contributing to the formation of reinforcing phases that enhance the overall performance of the material [42]. The XRD patterns in Fig. 9 reveal the presence of the white Al_2Cu phase and the grey Mg_2Si phase in the F2 sample, further enhancing the densification and strength, indicating good sintering performance and inter-bonding capability. In contrast, the Al−Mg−C carbides in the F1 sample and Al−Si−O oxides in the F3 sample inhibit the formation of Al_2Cu and Mg_2Si reinforcing phases, resulting in lower sintered

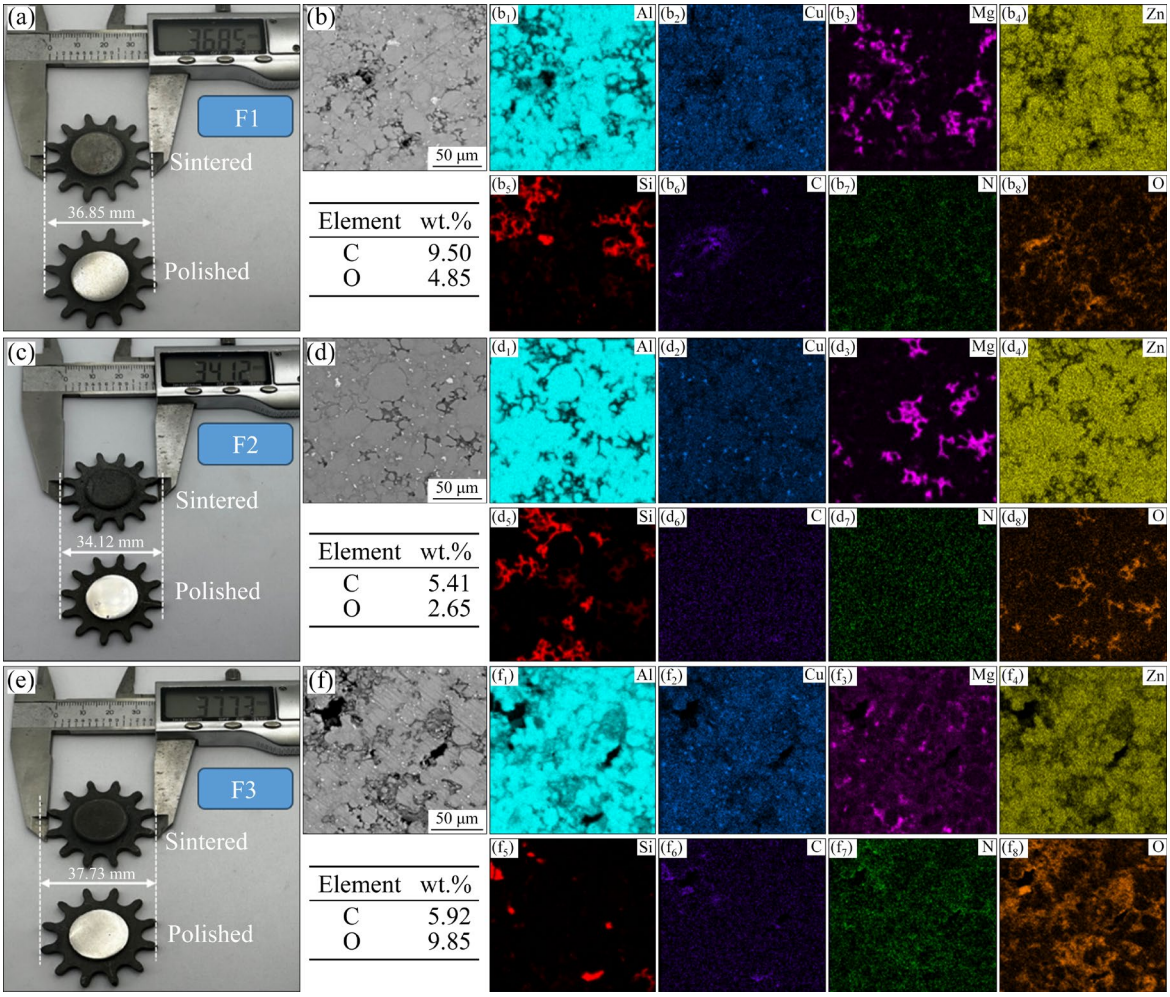

Fig. 8 Morphologies of 7075 Al alloy samples after sintering: (a) F1 macroscopic morphology; (b, b_1−b_8) SEM−EDS results of F1; (c) F2 macroscopic morphology; (d, d_1−d_8) SEM−EDS results of F2; (e) F3 macroscopic morphology; (f, f_1−f_8) SEM−EDS results of F3

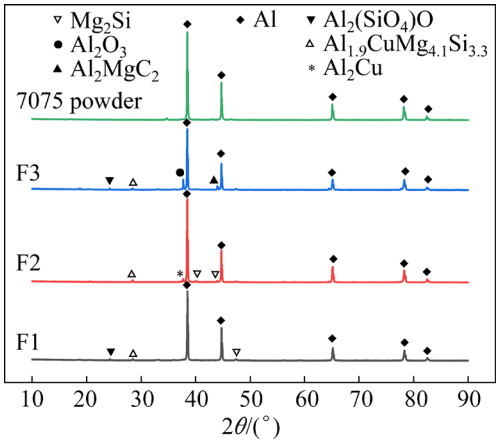

Fig. 9 XRD patterns of original alloy powder and three sets of sintered samples

densities for these groups. This suggests that an optimal phase composition can substantially enhance the mechanical properties of the materials.

3.5 C and O contents of sintered aluminum alloys

Figure 10 shows the C and O contents in the SEM images of the green bodies of the F1 and F3 groups after thermal debinding at different temperatures. As shown in Figs. 10(a) and (b), the raw billet was completely degreased at 500 °C, with no residual binder around the powder, and the C content in the F1 group increased to 11.98 wt.%. When the temperature reaches 540 °C, the C content increases to 12.18 wt.%, and the C element is uniformly distributed in the matrix. This uniform distribution leads to the aggregation of C at grain boundaries during the subsequent sintering process. Sintering densification of aluminum alloys is mainly controlled by grain boundary migration and grain growth. The aggregation of C at grain boundaries increases the diffusion barrier, which reduces the atomic diffusion rate and hinders the

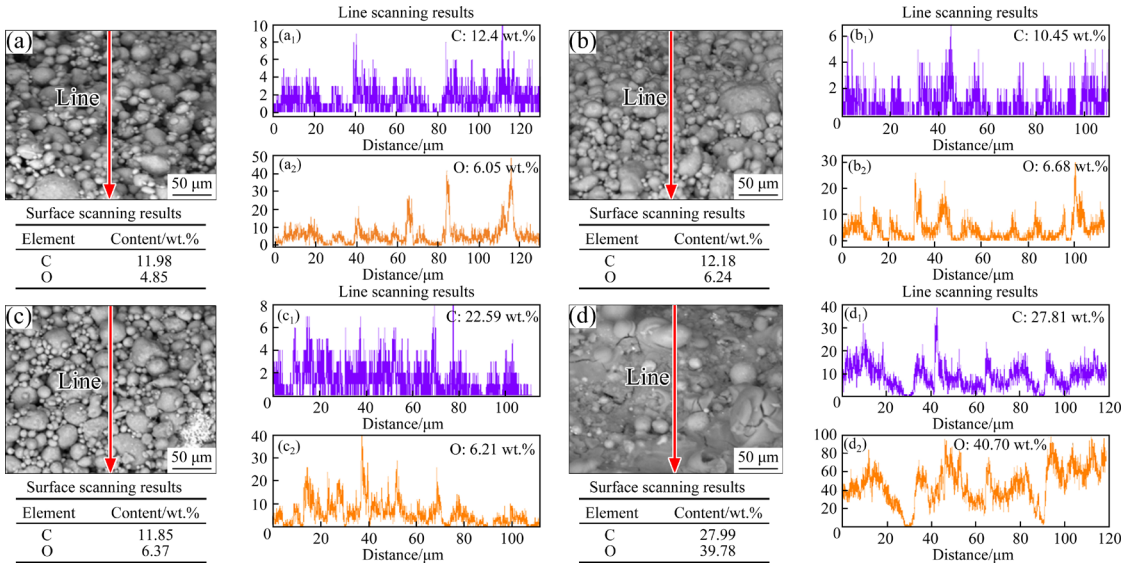

Fig. 10 SEM−EDS results of green bodies after thermal debinding at different temperatures: (a, a_1, a_2) F1, line scanning results at 500 °C; (b, b_1, b_2) F1, line scanning results at 540 °C; (c, c_1, c_2) F3, line scanning results at 500 °C; (d, d_1, d_2) F3, line scanning results at 540 °C

densification process [43,44]. In addition, the presence of C during the sintering process may lead to the formation of carbides, which can cause the formation of pores within the material. These pores are difficult to eliminate completely during sintering. Moreover, the pores may act as initiating points for cracks, reducing the overall strength of the material [45−47].

As shown in Figs. 10(c) and (d), the C content in the F3 group after debinding reaches 11.85 wt.%. Upon increasing the temperature to 540 °C, the C and O contents increase significantly. During the debinding process, although most of the EP resin is removed, some residual EP resin or its decomposition products may remain in the raw billet. Residual EP resin or its decomposition products can increase the C and O contents in the blank. Moreover, during the debinding process, the EP resin undergoes thermal or chemical decomposition, producing small molecular organic compounds that still contain significant amount of C and O. These decomposition products may become trapped in the pores or on the surface of the billet, thus increasing the C and O contents in the billet [48]. Excessively high C content hinders the sintering process, while high O content leads to secondary oxidation of the powder, forming a dense and stable oxide film on the surface of the alloy. This oxide film hinders the migration and diffusion process at grain boundaries, making it difficult to form sintering necks and, consequently, preventing densification [49,50]. The impediments of C and O to densification during sintering and the normal sintering densification process are shown in Fig. 11.

3.6 Preparation of complex shape components

Figure 12 presents a complex screw and gear component fabricated from an optimized F2 group feedstock. The blank surfaces are smooth and defect-free, featuring well-defined threads and gears with high dimensional accuracy. This result confirms the homogeneity of the optimized feedstock in terms of material distribution and density, demonstrating the effectiveness of the method in minimizing molding defects. Powder compression molding ensures the integrity and consistency of the original blanks during production, thereby avoiding cracks and porosity commonly associated with the conventional processes. Furthermore, the improved dimensional accuracy enables better part fit during subsequent machining and assembly, reducing the need for rework and minimizing material waste. This method not only boosts productivity but also lowers production costs, offering reliable technical support for large-scale manufacturing. The findings of this study confirm the potential of the compression molding process for a wide range of applications in producing complex parts, emphasizing its advantages in achieving high-precision, high-quality components.

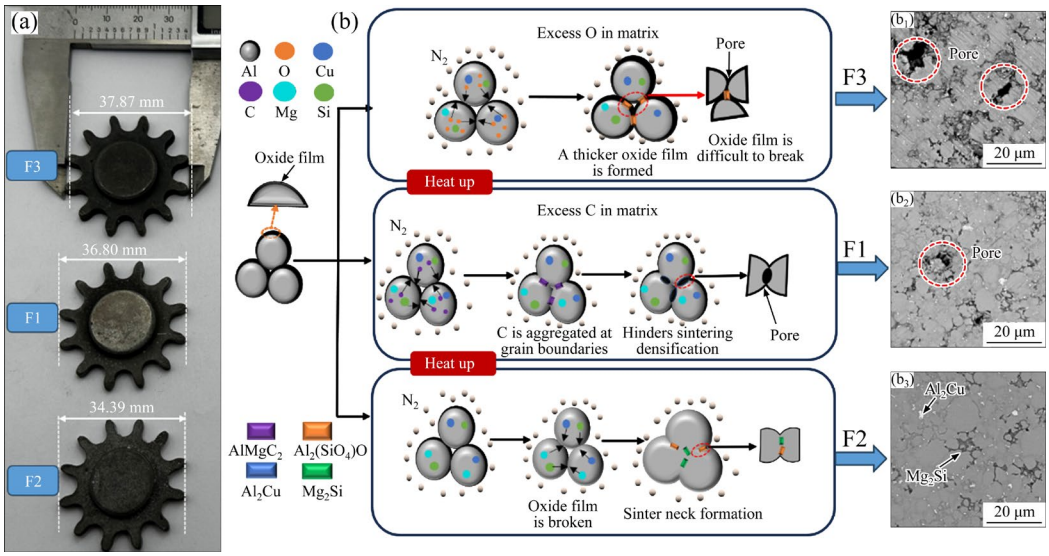

Fig. 11 Comparison of each sintered part (a) and sintering process with different C and O contents (b, b_1, b_2, b_3)

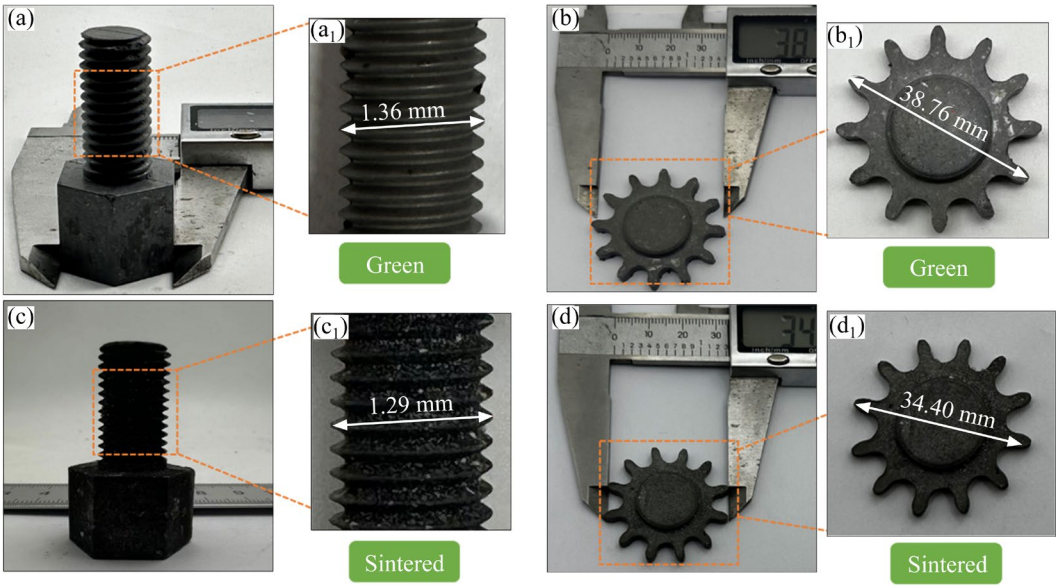

Fig. 12 Compression molding process for preparation of complex parts from F2 group feedstock: (a, a_1) Screw blanks; (b, b_1) Gear blanks; (c, c_1) Screw sintered parts; (d, d_1) Gear sintered parts

3.7 Mechanical properties

Table 2 shows the tensile strength of aluminum alloy injection molded parts in this study and literature [17,51,52]. The tensile strength of the F2 group samples reaches 193 MPa, significantly higher than that of aluminum alloys using wax-based binder systems. Table 3 shows the C and O contents of the three samples at various sintering temperatures. After the thermal debinding process, the C and O contents in F2 sample at 580 °C are lower than those in the other two groups, with values of 0.006 wt.% and 0.604 wt.%, respectively. The lower C and O contents reduce the formation of carbides and oxides during the sintering process, thereby optimizing the microstructure and mechanical properties of the sintered aluminium alloys. In contrast, the C content in F1 sample at 580 °C increased to 0.309 wt.%, while O content rose to 1.630 wt.%, whereas in F3 sample at 580 °C, C content increased to 0.292 wt.% and O content to 2.515 wt.%. The increase in C and O contents impedes the subsequent sintering process, resulting in lower densities of the samples in these two groups.

Figure 13 presents SEM images for the tested samples. F1 group samples have a significant

Table 2 Comparison of performance of aluminum alloy injection molded components in this study and literature

Sample	Tensile strength/MPa	Shrinkage rate/%	Relative density/%	Source
F1	102±15	3.76±0.18	85.52	This work
F2	193±20	4.24±0.21	97.64	This work
F3	48±13	2.55±0.15	79.01	This work
Al−Si	154	−	95.50	Ref. [17]
6061Al+ 2wt.%Sn+ 10wt.%AlN	184	−	970	Ref. [51]
6061Al+ 2wt.%Sn	165	−	97.10	Ref. [52]

Table 3 C and O contents of three samples at different temperatures

Sample	C content/wt.%			O content/wt.%		
	500 °C	540 °C	580 °C	500 °C	540 °C	580 °C
F1	0.215	0.478	0.309	0.498	0.943	1.630
F2	0.197	0.192	0.006	0.762	0.951	0.604
F3	0.320	0.384	0.292	0.861	1.186	2.515

number of pores, which suggests that excessive C at the grain boundaries significantly hinders the diffusion process during sintering. Additionally, Figs. 13(e) and (f) illustrate that the F3 group samples display a higher pore density and pronounced powder agglomeration. This indicates that the excessive oxygen causes the secondary oxidation of the aluminum alloy powders in F3 group

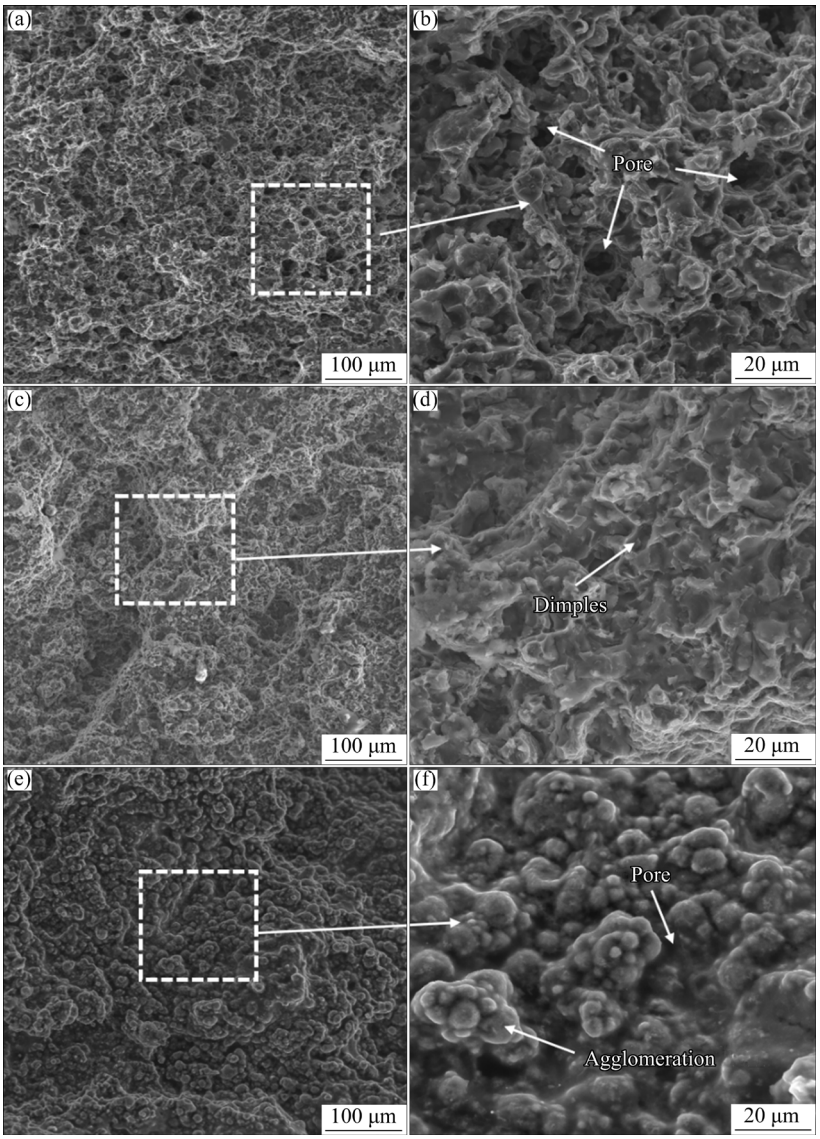

Fig. 13 SEM images of fracture surface of sintered samples after tensile strength test: (a, b) F1; (c, d) F2; (e, f) F3

sample, thereby hindering the formation of sintering necks between the particles. Figures 13(c) and (d) display SEM images of the fracture surfaces of F2 samples. The grain size of the sintered samples is approximately 10 μm, and the fracture surfaces show the presence of dimples and tearing edges. Hence, the material has good plastic deformation capability and exhibits a ductile fracture mode. The dense distribution of dimples and the reduced presence of voids on the fracture surface further indicate that the material sintered in this composition achieves greater density and improved mechanical properties.

4 Conclusions

(1) Additives can promote the intermolecular or intramolecular interactions between the powder and binder, and improve the compatibility between them, in which the contact angle between 7075 powder and POM is 106.6° when EBS is used. Meanwhile, the feedstock shows a lower non-newtonian index of 0.25.

(2) EBS is suitable to be used as an additive in 7075-POM based feedstocks. The lowest C and O contents in the sintered F2 samples accelerate the formation of intermediate phases such as Al_2Cu and Mg−Si compounds. When DOP and EP were used as additives, the C and O contents of the samples should be too high to impede the sintering process.

(3) Geometrically complex 7075 aluminium alloy with a high relative density of 97.64% and a tensile strength of 193 MPa was prepared by high nitrogen-flow sintering method.

CRediT authorship contribution statement

Heng ZOU: Conceptualization, Resources, Writing − Original draft; **Meng-xiong CHEN:** Validation, Methodology; **Yang FU:** Investigation, Formal analysis; **Hui-wen XIONG:** Funding acquisition, Writing − Reviewing & editing; **Lei ZHANG:** Project administration, Software; **Ke-chao ZHOU:** Supervision, Data curation.

Declaration of competing interest

The authors declare that they have no known competing financial interests or personal relationships that could have appeared to influence the work reported in this paper.

Acknowledgments

This research was supported by the National Key Research and Development Program of China (No. 2021YFB3701900).

Supplementary materials

Supplementary materials in this paper can be found at: http://tnmsc.csu.edu.cn/download/04-p3862-2024-0933-Supplementary_Materials.pdf.

References

[1] SATHISH T, SARAVANAN R, KUMAR A, CHANDER P, MOHD S, MANISH G SENTHILKUMAR N, PANDIT B, UBAIDULLAH M, SMIRNOV V A. Influence of synthesizing parameters on surface qualities of aluminium alloy AA5083/CNT/MoS_2 nanocomposite in powder metallurgy technique [J]. Journal of Materials Research and Technology, 2023, 27: 1611−1629.

[2] NOVAK P, BENEDIKTOVA D, MESTEK S, TSEPELEVA A, KOPECEK J. Aluminum alloys with natural ratio of alloying elements manufactured by powder metallurgy [J]. Journal of Alloys and Compounds, 2023, 931: 167440.

[3] WU Lei, ZHAO Ji-yu, LIU Chao, MA Yun-zhu, HUANG Yu-feng, WANG Tao, YANG Lun, YANG Huan-yuan, LIU Wen-sheng. Microstructure and tensile properties of aluminum powder metallurgy alloy prepared by a novel low-pressure sintering [J]. Journal of Materials Research and Technology, 2021, 14: 1419−1429.

[4] DEHGHAN-MANSHADI A, BERMINGHAM M J, DARGUSCH M S, STJOHN D H, QIAN M. Metal injection moulding of titanium and titanium alloys: Challenges and recent development [J]. Powder Technology, 2017, 319: 289−301.

[5] WIDYASTUTI, FALAH E, PRATIWI V, ADITYAWAN I, SAFRIDA N, WIKANDARI E, WIDIYANTO A R, ABDULLAH R. Research progress, potentials, and challenges of copper composite for metal injection moulding feedstock [J]. Powder Technology, 2024, 440: 119785.

[6] WIRATKAPUN K, SUWANPREECHA C, LINJEE S, SONGKUEA S, WUTIKHUN T, YORDSRI V, MANONUKUL A. Surface modification and enhanced wear performance through severe shot peening treatment in 316L stainless steel manufactured by metal injection moulding [J]. Journal of Materials Research and Technology, 2024, 29: 4072−4085.

[7] SHU Chang, HE Hao, FAN Bo-wen, LI Jie-hua, WANG Tao, LI Dong-yang, LI Yi-min, HE Hao. Biocompatibility of vascular stents manufactured using metal injection molding in animal experiments [J]. Transactions of Nonferrous Metals Society of China, 2022, 32(2): 569−580.

[8] WEI Li-jun, HAN Bao-shuai, YE Fan, DITTA A, LI Long, XU Yan-jin, WU Su-jun. Influencing mechanisms of heat treatments on microstructure and comprehensive properties of Al−Zn−Mg−Cu alloy formed by spray forming [J]. Journal of Materials Research and Technology, 2020, 9(3): 6850−6858.

[9] LIM K, HAYAT M D, JENA K D, YUAN Zhen-tao, LI Lu, CAO Peng. Formulating titanium powder feedstocks for

metal injection moulding from a clean binder system [J]. Powder Technology, 2024, 433: 119214.

[10] WANG Tao, HUANG Yu-feng, YANG Lun, MA Yun-zhu, LIU Chao, WU Lei, YAN Huan-yuan, ZHAO Xin-yue, LIU Wen-sheng. Microstructure and mechanical properties of 7055 Al alloy prepared under different sintering conditions using powder by-products [J]. Materials Science and Engineering A, 2021, 805: 140562.

[11] CHEN Meng-xiong, XIONG Hui-wen, FU Yang,ZOU Heng, KANG Xiao, ZHANG Lei, ZHOU Ke-chao. Fabrication of large cross-section Ti−6Al−4V alloy using EBS-modified POM-based feedstock [J]. Powder Technology, 2024, 434: 119364.

[12] QI Xing, TAKATA N, SUZUKI A, KOBASHI M, KATO M. Controllable tensile performance of additively manufactured Al−Fe alloy [J]. Materials Science and Engineering A, 2022, 855: 143893.

[13] LI Jin-peng, ZHANG Hua-rui, HU Shuang-long, DU Ming, JIN Yu, CHEN Jiu-long, ZHANG Hu, CHENG Ying. Effects of surfactants on the physical properties of silicate binders and the mechanical properties of silicate-bonded foundry sand cores [J]. Ceramics International, 2024, 50(17): 30637−30646.

[14] ZHANG Yu-bo, WANG Wei, LIU Jia-jiang, WANG Tong-min, LI Ting-ju. Fabrication of carbon fiber reinforced aluminum matrix composites by inorganic binders [J]. Journal of Alloys and Compounds, 2023, 968: 172213.

[15] ZHANG Tian, TAN Yun-qiang, XU Yang-Li, LIU Chao. A thermal-initiated monomer binder enhancing green strength with low binder saturation for binder jetting additive manufacturing of cemented carbide [J]. International Journal of Refractory Metals and Hard Materials, 2024, 118: 106494.

[16] CHEN Hui, ZENG Zhe, WEI Zi-yao, WANG Rui, ZHANG Run-hua. Assessment of the effectiveness of binder fatigue, rheology and chemistry parameters in evaluating cracking resistance in high RAP mixtures modified with recycling agents [J]. Construction and Building Materials, 2024, 432: 136572.

[17] NI Jia-qi, YU Mu-hao, HAN Ke-qing. Debinding and sintering of an injection-moulded hypereutectic Al−Si alloy [J]. Materials, 2018, 11(5): E807.

[18] DAYAM S, TANDON P, PRIYADARSHI S. Development of paste extrusion-based metal additive manufacturing process [J]. Rapid Prototyping Journal, 2022, 28(10): 1920−1932.

[19] GILMER D, KIM S J, GOLDSBY D J, NANDWANA P, ELLIOTT A, SAITO T. Predictive binder jet additive manufacturing enabled by clean burn-off binder design [J]. Additive Manufacturing, 2024, 80: 103955.

[20] DONG Bo-lun, CAI Xiao-yu, LIN San-bo, LI Xiao-long, FAN Chen-lei, YANG Chun-li, SUN Hao-ran. Wire arc additive manufacturing of Al−Zn−Mg−Cu alloy: Microstructures and mechanical properties [J]. Additive Manufacturing, 2020, 36: 101447.

[21] SUN Zhi-yuan, QIN Min-li, LI Rui, MA Ji-dong, FANG Fei, LU Hui-feng, QU Xuan-hui. Preparation of high performance soft magnetic alloy Fe−4Si−0.8P by metal injection molding [J]. Advanced Powder Technology, 2017, 28(10): 2687−2693.

[22] WANG Yi-peng, ZHANG Shuo, LI Hong, ERIKA H, LI Zhuo-xin, CONG Bao-qiang. Microstructure and mechanical properties of 7075/5356 aluminum alloy laminated composite fabricated by wire arc additive manufacturing [J]. Materials Letters, 2024, 367: 136638.

[23] MURUGABALAJI V, ROUT M, SONI H, SAHOO B N. Corrosion characteristics of AA 7075 and AA 7075/SiC/Gr hybrid composite processed through multistep hot cross rolling [J]. Materials Chemistry and Physics, 2024, 313: 128713.

[24] FENG Man, WU Qin-li, XUE Jing, LUO Zhen-jiao, WANG Zhi-ping, AN Xiang-hai, LIAO Xiao-zhuo, LI Jie-hua, JIN Shen-bao, SHA Gang. High-pressure-torsion-induced segregation, precipitation and grain refinement of Al−(Si, Mg and Cu) binary alloys [J]. Journal of Materials Science & Technology, 2024, 199: 102−113.

[25] DANG Wen-long, WANG Li-min, YANG Zhen-liang, WANG Lin-shan, WANG Li-gen, LIANG Xue-bing. Effect of sintering atmosphere and temperature on the properties of AlCuMgSi alloys [J]. Powder Metallurgy Materials Science and Engineering, 2014, 19(6): 921−927.

[26] LIU Chun-lin, ZHANG Qian-peng, LU Yin, SHI An-kang, LIU Gang, WU Dun. Effect of surfactants on the compatibility of Ti−6Al−4V metal injection moulding feedstocks [J]. Polymer Materials Science and Engineering, 2018, 34(9): 96−100.

[27] CHEN Meng-xiong, XIONG Hui-wen, ZHANG Lei, KANG Xiao, LI Zhi-you, ZHOU Ke-chao. Complex-shaped TiC/Ti(C,N)-based cermet prepared via rheological press molding using highly-filled granular feedstock [J]. International Journal of Refractory Metals and Hard Materials, 2023, 115: 106281.

[28] SCHAFFER G B, HALL B J, BONNER S J, HUO S H, SERCOMBE T B. The effect of the atmosphere and the role of pore filling on the sintering of aluminium [J]. Acta Materialia, 2006, 54(1): 131−138.

[29] CHEN Meng-xiong, YI Zhong-huai, XIONG Hui-wen, ZOU Heng, KANG Xiao, ZHANG Lei, ZOU Jian-peng, ZHOU Ke-chao. Efficient catalytic debinding feedstock design for material extrusion additive manufacturing of low warpage and high-density titanium alloy [J]. Applied Materials Today, 2024, 40: 102383.

[30] SUN Yi, ZOU Heng, YI Zhong-huai, XIONG Hui-wen, KANG Xiao, ZHANG Lei, ZHOU Ke-chao. Material extrusion of high-density SiC_p/7075Al composite via a high nitrogen-flowing assisted sintering [J]. Materials Characterization, 2024, 214: 114113.

[31] BIESINGER M C, PAYNE B P, GROSVENOR A, LAU L W M, GERSON A, SMART R S. Resolving surface chemical states in XPS analysis of first row transition metals, oxides and hydroxides: Cr, Mn, Fe, Co and Ni [J]. Applied Surface Science, 2011, 257(7): 2717−2730.

[32] TAMURA H, MITA K, TANAKA A, ITO M. Mechanism of hydroxylation of metal oxide surfaces [J]. Journal of Colloid and Interface Science, 2001, 243(1): 202−207.

[33] SMITH M B, MARCH J. March's advanced organic chemistry: Reactions, mechanisms, and structure [M]. 7th ed. New Jersey: Wiley-Interscience, 2007.

[34] DESIRAJU G, STEINER T. The weak hydrogen bond in structural chemistry and biology [M]. Oxford: Oxford Academic, 2001.

[35] SUN Yi, YI Zhong-huai, SHEN Ting, XIONG Hui-wen, KANG Xiao, ZHANG Lei, ZHOU Ke-chao. Microstructure and mechanical properties of 7075 aluminum alloy prepared

by metal fused deposition modeling [J]. Transactions of Nonferrous Metals Society of China, 2024, 34(7): 2108−2119.
[36] VO Q V, THAO L T T, MANH T D, BAY M V, TRUONG-LE B T, HOA N T, MECHLER A. Reaction of methylene blue with OH radicals in the aqueous environment: Mechanism, kinetics, products and risk assessment [J]. RSC Advances, 2024, 14(37): 27265−27273.
[37] NAKAMURA S, TSUJI Y, YOSHIZAWA K. Role of hydrogen-bonding and OH−π interactions in the adhesion of epoxy resin on hydrophilic surfaces [J]. ACS Omega, 2020, 5(40): 26211−26219.
[38] LANGLAIS D, DEMERS V, BRAILOVSKI V. Rheology of dry powders and metal injection molding feedstocks formulated on their base [J]. Powder Technology, 2022, 396: 13−26.
[39] HUANG Bai-yun, LIANG Shu-quan, QU Xuan-hui. The rheology of metal injection molding [J]. Journal of Materials Processing Technology, 2003, 137(1/2/3): 132−137.
[40] LIN Bo, HE Xiang-xiang, XIA Song-chao, XIAO Hua-qiang, ZHAO Yu-liang, KHANLARI K. Effect of ultrasonic and mechanical vibration treatments on evolution of Mn-rich phases and mechanical properties of Al−12Si−4Cu−1Ni−1Mg−2Mn piston alloys [J]. Transactions of Nonferrous Metals Society of China, 2024, 34(8): 2393−2414.
[41] TANG Hao, GENG Yao-xiang, GAO Chao-feng, XI Xiao-ying, ZHANG Jian-tao, XIAO Zhi-yu. Microstructure evolution and mechanical properties of high-performance Al−Mn−Mg−Sc−Zr alloy fabricated by laser powder bed fusion [J]. Transactions of Nonferrous Metals Society of China, 2024, 34(5): 1413−1426.
[42] YANG Yu-tong, HUANG Shi-yao, ZHENG Jiang, YANG Li, CHENG Xiao-nong, CHEN Rui-kai, HAN Wei-jian. Effect of porosity and α-Al(Fe/Mn)Si phase on ductility of high-pressure die-casting Al−7Si−0.2Mg alloy [J]. Transactions of Nonferrous Metals Society of China, 2024, 34(2): 378−391.
[43] DENG Xiang-xing, ZHENG Ruo-nian, TORRALBA J M, ANDREA G J, WANG Yang-wei. Effect of C content on microstructure and mechanical properties of Cr-based hard composites obtained by different sintering methods [J]. Materials Science and Engineering A, 2022, 848: 143377.
[44] LI Ao-xiang, KANG Kai-wen, XU Su, ZHANG Jin-shan, HUANG Di, CHE Chun-ning, LI Ya-qing, XU Ming-kun, LIU Sai-ke, JIANG Yi-teng, LI Gong. Effect of C content on microstructure evolution and mechanical properties of $CoCrFeNiTa_{0.1}$ high entropy alloy [J]. Journal of Alloys and Compounds, 2024, 23: 175318.
[45] WANG H, WANG Cun-yu, LIANG Jian-xiong, GODFREY A, WANG Yu-hui, WENG Yu-qing, CAO Wen-quan. Effect of alloying content on microstructure and mechanical properties of Fe−Mn−Al−C low-density steels [J]. Materials Science and Engineering A, 2023, 886: 145675.
[46] GAL W C, SONG G W, BAEK W H, KIM H K, LEE D K, PARK S J. Fabrication of pressureless sintered Si_3N_4 ceramic balls by powder injection molding [J]. Ceramics International, 2019, 45(5): 6418−6424.
[47] DU Zhi-yuan, WU Mao, QIU Ting-ting, QU Xuan-hui. Injection molding of Al−Cu−Mg−Si system aluminum alloys [J]. Transactions of Nonferrous Metals Society of China, 2019, 29(11): 2471−2481.
[48] QIU Ting-ting, WU Mao, DU Zhi-yuan, QU Xuan-hui. Powder metallurgy aluminum alloy sintering densification process [J]. Journal of Engineering Science, 2018, 40(9): 1075−1082.
[49] JIA Zhi-hong, ZHOU Guang-wen, ZHOU Hong-yu, LIU Fei, DING Li-peng, WENG Yao-yao, XIANG Kai-yun, ZHAO Hai-dong. Effects of Cu content and heat treatment process on microstructures and mechanical properties of Al−Si−Mg−Mn−xCu cast aluminum alloys [J]. Transactions of Nonferrous Metals Society of China, 2024, 34(3): 737−754.
[50] MUTHUCHAMY A, SRIKANTH M, AGRAWAL D K, ANNAMALAI A R. Effect of microwave and conventional modes of heating on sintering behavior, microstructural evolution and mechanical properties of Al−Cu−Mn alloys [J]. Molecules, 2021, 26(12): 3675.
[51] LIU Z Y, KENT D, SCHAFFER G B. Powder injection moulding of an Al−AlN metal matrix composite [J]. Materials Science and Engineering A, 2009, 513/514: 352−356.
[52] LIU Z Y, SERCOMBE T B, SCHAFFER G B. Metal injection moulding of aluminium alloy 6061 with tin [J]. Powder Metallurgy, 2008, 51(1): 78−83.

改性聚甲醛基喂料制备复杂形状 7075 铝合金的显微组织和力学性能

邹 恒，陈梦熊，付 杨，熊慧文，张 雷，周科朝

中南大学 粉末冶金国家重点实验室，长沙 410083

摘 要：以邻苯二甲酸二辛酯(DOP)、乙撑双硬脂酰胺(EBS)和环氧树脂(EP)为添加剂修饰 7075 Al 合金粉末表面。DOP 和 EBS 中的官能团与 Al 粉末表面的羟基形成氢键。此外，环氧树脂中的环氧基团与羟基发生开环反应。上述相互作用增加了合金粉末与聚甲醛(POM)之间的相容性。烧结后，含 DOP 和 EP 的样品中 C、O 含量较高，而含 EBS 添加剂的样品具有最低的 C、O 含量，分别为 0.006% C (质量分数)和 0.604% O (质量分数)。在烧结过程中，过量的 C 倾向于积聚在晶界处。同时，过量的 O 会导致铝合金粉末的二次氧化，从而抑制烧结致密化过程。因此，含有 DOP 和 EP 的样品致密度分别仅为 85.52%和 79.01%。相比之下，以 EBS 作为添加剂时可获得相对密度为 97.64%、抗拉强度为 193 MPa 的高质量铝合金零件。

关键词：7075 铝合金；聚甲醛基喂料；添加剂；压缩成型；金属注射成型；显微组织；力学性能

(Edited by Wei-ping CHEN)